Article

Clustering Analysis on Drivers of O$_3$ Diurnal Pattern and Interactions with Nighttime NO$_3$ and HONO

Xue Wang [1], Shanshan Wang [1,2,*], Sanbao Zhang [1], Chuanqi Gu [1], Aimon Tanvir [1], Ruifeng Zhang [1] and Bin Zhou [1,2,3,*]

1 Shanghai Key Laboratory of Atmospheric Particle Pollution and Prevention (LAP3), Department of Environmental Science and Engineering, Fudan University, Shanghai 200438, China; 19210740059@fudan.edu.cn (X.W.); 21110740022@m.fudan.edu.cn (S.Z.); 19210740067@fudan.edu.cn (C.G.); 19110740045@fudan.edu.cn (A.T.); 17110740025@fudan.edu.cn (R.Z.)
2 Institute of Eco-Chongming (IEC), No. 20 Cuiniao Road, Shanghai 202162, China
3 Institute of Atmospheric Sciences, Fudan University, Shanghai 200433, China
* Correspondence: shanshanwang@fudan.edu.cn (S.W.); binzhou@fudan.edu.cn (B.Z.)

Abstract: The long-path differential optical absorption spectroscopy (LP-DOAS) technique was deployed in Shanghai to continuously monitor ozone (O$_3$), formaldehyde (HCHO), nitrogen dioxide (NO$_2$), nitrous acid (HONO), and nitrate radical (NO$_3$) mixing ratios from September 2019 to August 2020. Through a clustering method, four typical clusters of the O$_3$ diurnal pattern were identified: high during both the daytime and nighttime (cluster 1), high during the nighttime but low during the daytime (cluster 2), low during both the daytime and nighttime (cluster 3), and low during the nighttime but high during the daytime (cluster 4). The drivers of O$_3$ variation for the four clusters were investigated for the day- and nighttime. Ambient NO caused the O$_3$ gap after midnight between clusters 1 and 2 and clusters 3 and 4. During the daytime, vigorous O$_3$ generation (clusters 1 and 4) was found to accompany higher temperature, lower humidity, lower wind speed, and higher radiation. Moreover, O$_3$ concentration correlated with HCHO for all clusters except for the low O$_3$ cluster 3, while O$_3$ correlated with HCHO/NO$_x$, but anti-correlated with NO$_x$ for all clusters. The lower boundary layer height before midnight hindered O$_3$ diffusion and accordingly determined the final O$_3$ accumulation over the daily cycle for clusters 1 and 4. The interactions between the O$_3$ diel profile and other atmospheric reactive components established that higher HONO before sunrise significantly promoted daytime O$_3$ generation, while higher daytime O$_3$ led to a higher nighttime NO$_3$ level. This paper summarizes the interplays between day- and nighttime oxidants and oxidation products, particularly the cause and effect for daytime O$_3$ generation from the perspective of nighttime atmospheric components.

Keywords: ozone pollution; photochemical reaction; nighttime ozone; clustering; LP-DOAS

1. Introduction

In the troposphere, the photochemical reactions of nitrogen oxides (NO$_x$) and volatile organic compounds (VOCs) act as major yield factors for ozone (O$_3$) [1]. In addition, regional transport and tropospheric intrusion also contribute to stratospheric O$_3$ levels [2]. As an important product of photochemical reactions, O$_3$ actively participates in certain atmospheric chemical processes. The strong oxidation potential of O$_3$ renders it not only harmful for animals and plants [3], but also a crucial driver for climate change [4] and ecosystem damage [5]. Severe O$_3$ pollution episodes have repeatedly been reported over China in recent years [6,7]. In order to regulate and control tropospheric O$_3$ formation, it is imperative to understand the drivers that integrate to cause changes in tropospheric O$_3$ levels. Principally, surface concentrations of O$_3$ are dominated by anthropogenic precursors and meteorological conditions [8]. In densely populated and economic zones such as eastern China, O$_3$ pollution is severe because of the higher emissions of VOCs and NO$_x$ [9].

With respect to meteorological conditions, temperature, humidity, wind and sunshine duration, etc., have been identified as having crucial effects on O_3 concentration [10–12].

In addition to directly analyzing O_3 pollution characteristics from the available observational results, adoption of various models to simulate O_3 budgets, such as the Box model [13] and RACM2-LIM1 [14], has become prevalent as an advanced study approach to characterizing regional O_3 pollution. Regardless of the approach used, much of the focus is on the photochemical generation of O_3 during the daytime. There are very few studies that report the drivers of nighttime variations in O_3, especially its interactions with the reactive atmospheric components (such as NO_3 and HONO) apart from the key meteorological factors.

Differential optical absorption spectroscopy (DOAS) is a common technique used to measure the concentrations of trace gases and radicals in the atmosphere [15] and has been widely applied in atmospheric pollution monitoring [16]. This technique not only enables long-term continuous automatic observation with a single set of equipment, but also allows for the simultaneous measurement of multiple pollutants owing to different absorption properties for different pollutant gases [17]. The concentrations of O_3 as well as the relevant atmospheric components, including HCHO, NO_2, HONO, and NO_3, are captured synchronously with DOAS, which greatly reduces the errors caused by measurements with multiple instruments. Furthermore, the DOAS measurement capability enriches our scope in the survey of O_3 pollution.

The current study is structured as follows. Section 2 describes the instrument specifications and methodology. The results of DOAS observation are overviewed in Section 3.1. In Section 3.2, we group O_3 pollution into four clusters by clustering method according to different diurnal patterns. The drivers of the differences among the four clusters are studied based on the relevant atmospheric components and meteorological factors during three periods: daytime, before, and after midnight. In Section 3.3, we discuss the interactions between day- and nighttime atmospheric components to further interpret the causes and impacts of daytime O_3 pollution.

2. Measurement and Method

2.1. Measurement Site and Instrument Installation

A long-path DOAS (LP-DOAS) instrument was installed in Nanhui (121.80° E, 31.06° N), which is a suburb located east of Shanghai, China, about 10 km from the East China Sea coastline (Figure 1). Although several point sources of pollution such as the Laogang Chemical Industrial Park to the east and the Pudong International Airport to the north surround this site, heavy traffic emissions hardly occur. Overall, the area maintains lower levels of observed NO_x, but nearly identical levels of O_3 compared with the urban areas.
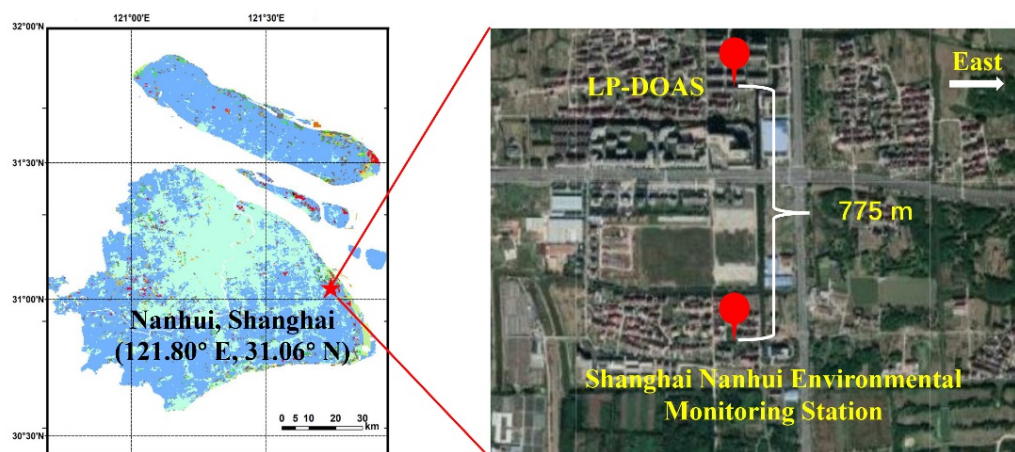

Figure 1. The topographic locations of the LP-DOAS instrument and Shanghai Nanhui Environmental Monitoring Station (© Google Earth).

In order to monitor several different species synchronously, two collocated LP-DOAS systems were arranged for ultraviolet and visible wavelength ranges. Each LP-DOAS system consisted of the light source (150 W Xenon lamp for ultraviolet, light-emitting diode lamp for visible light), a light-emitting/receiving system with the telescope diameter of 210 mm, a spectrometer with a photodiode array detector (1024 pixels), and a computer as the controller. The instrument was mounted on the sixth floor of a residential building about 19 m above the ground. The retroreflector shared by the two systems was installed on the roof of the Shanghai Nanhui Environmental Monitoring Station, 775 m away from the observation site. The collimating beam emitted by the light source was reflected by the retroreflector after a certain distance transmission and finally collected by the receiving port. Afterwards, the light signals processed by the spectrometer were converted into electrical signals and recorded on the computer. In addition, the dark current and noise were removed during the measurement process by blocking the light emitted by the lamp and alternately collecting the background spectrum. The temporal resolution of spectral acquisition was six minutes.

2.2. Spectral Analysis

DOAS is based on the Beer–Lambert law, which describes the relationship between the intensity of light absorption and the concentration of the light-absorbing substance of a certain wavelength. According to various differential absorption characteristics, the concentrations of O_3, HCHO, NO_2, and HONO in the atmosphere were retrieved through the observed ultraviolet spectra [18], while the concentration of NO_3 was retrieved by visible spectra [19].

The spectral retrieval was mainly performed using DOASIS software developed by the Institute of Environmental Physics at Heidelberg University. For this study, the spectral analysis settings and detection limits of O_3, HCHO, NO_2, HONO, and NO_3 retrieval are shown in Table S1. The high-resolution absorption cross-sections of NO_2 [20], HCHO [21], SO_2 [22], HONO [23], O_3 [24], H_2O (from the HITRAN database), and solar spectra were included in the fitting process. The theoretical detection limits are 2.0 ppbv for O_3, 0.1 ppbv for HCHO and HONO, 1 ppbv for NO_2, and 4 pptv for NO_3.

Figure 2 presents typical DOAS spectral fitting results for O_3, HCHO, NO_2, HONO, and NO_3. Moreover, the spectral retrieval results with residuals higher than 4×10^{-4} for HCHO, NO_2, HONO, and NO_3, and higher than 2×10^{-3} for O_3 were filtered out. More than 90% of the results passed the filter, indicating the good performance of the DOAS spectral fitting. Additionally, intercomparison of O_3 and NO_2 measured by DOAS and in-situ instruments at the Shanghai Nanhui Environmental Monitoring Station verified the reliability of the DOAS measurements fitting as well ($R^2 > 0.9$ for both) (Figure S1). The spectral fitting results within 1 h intervals were averaged for the following discussion.

2.3. Auxiliary Data

The time series of nitric oxide (NO) was obtained from the Shanghai Nanhui Environmental Monitoring Station, of which the temporal resolution was 1 h. All of the meteorological parameters used in this study, including temperature, relative humidity, wind, surface radiation, and boundary layer height, were obtained from the ERA5 data set of the European Centre for Medium-Range Weather Forecasts.
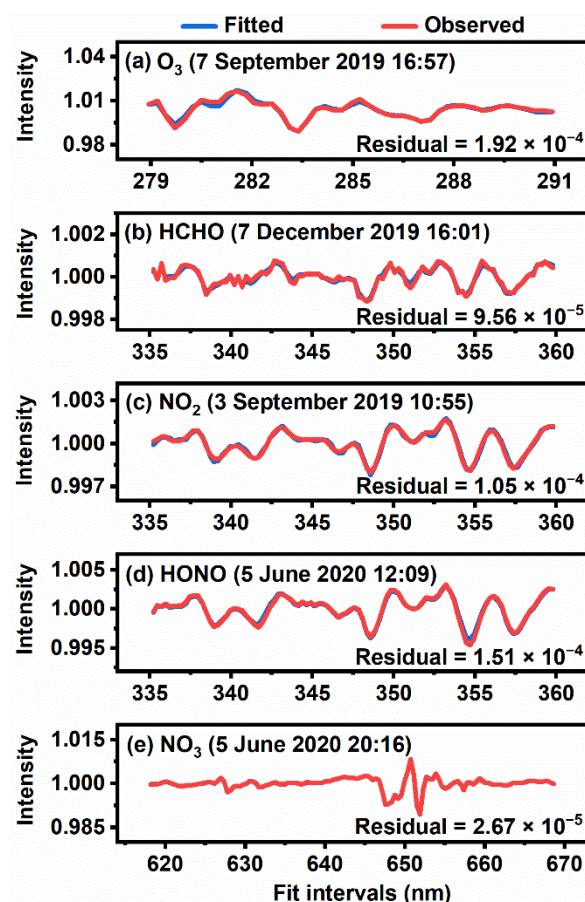
Figure 2. Examples of typical DOAS spectral fitting results for O_3 (**a**), HCHO (**b**), NO_2 (**c**), HONO (**d**), and NO_3 (**e**) including the observed and fitted result.

3. Results and Discussion

3.1. Overview of Observation

The monthly box charts of the daily means for O_3, HCHO, NO_2, HONO and NO_3 measured by LP-DOAS from September 2019 to August 2020 are shown in Figure 3. The annual means of O_3, HCHO, NO_2, HONO, and NO_3 were 34.33 ppbv, 2.41 ppbv, 12.77 ppbv, 0.61 ppbv and 9.34 pptv, respectively. Overall, the trend of monthly O_3 averages presented a single peak during the year with a maximum of 40.56 ppbv and a minimum value of 17.00 ppbv in May 2020 and December 2019, respectively. This was a prominent reduction compared with 2014 to 2018 [25], indicating the remarkable delayed benefits of the continuous Clean Air Action Plan in China. It has been reported that O_3 concentrations increased sharply in megacities with the implementation of the Clean Air Action Plan in 2013, but decreased after about three or four years later [26–28]. In addition, the Meiyu period in June and July of 2020 caused lower surface O_3 concentrations, so it was not surprising that the O_3 peaked in May 2020. Nevertheless, many higher O_3 pollution episodes still occurred in summer even though the means were reduced, as displayed by the short lines of the 90th percentile in the box chart (Figure 3a).

Likewise, the variations in the mean HCHO concentrations revealed a single-peak trend throughout the year, with a maximum of 4.60 ppbv in July 2020 and a minimum of 1.20 ppbv in February 2020. The concentration of HCHO was comparable to the observation in summer 2018 in Shanghai reported by Guo et al. (2021) [29]. Compared to O_3 and HCHO, NO_2 and HONO depicted an opposite variation, the overall levels of both in 2019 were significantly higher than those in 2020. After December 2019, both dropped rapidly in January and February 2020, exhibiting a greater decline relative to the values in previous

years [30,31]. This phenomenon is due to the COVID-19 lockdown in early 2020, which led to the reductions in anthropogenic activities and hence the pollutant emissions [32].
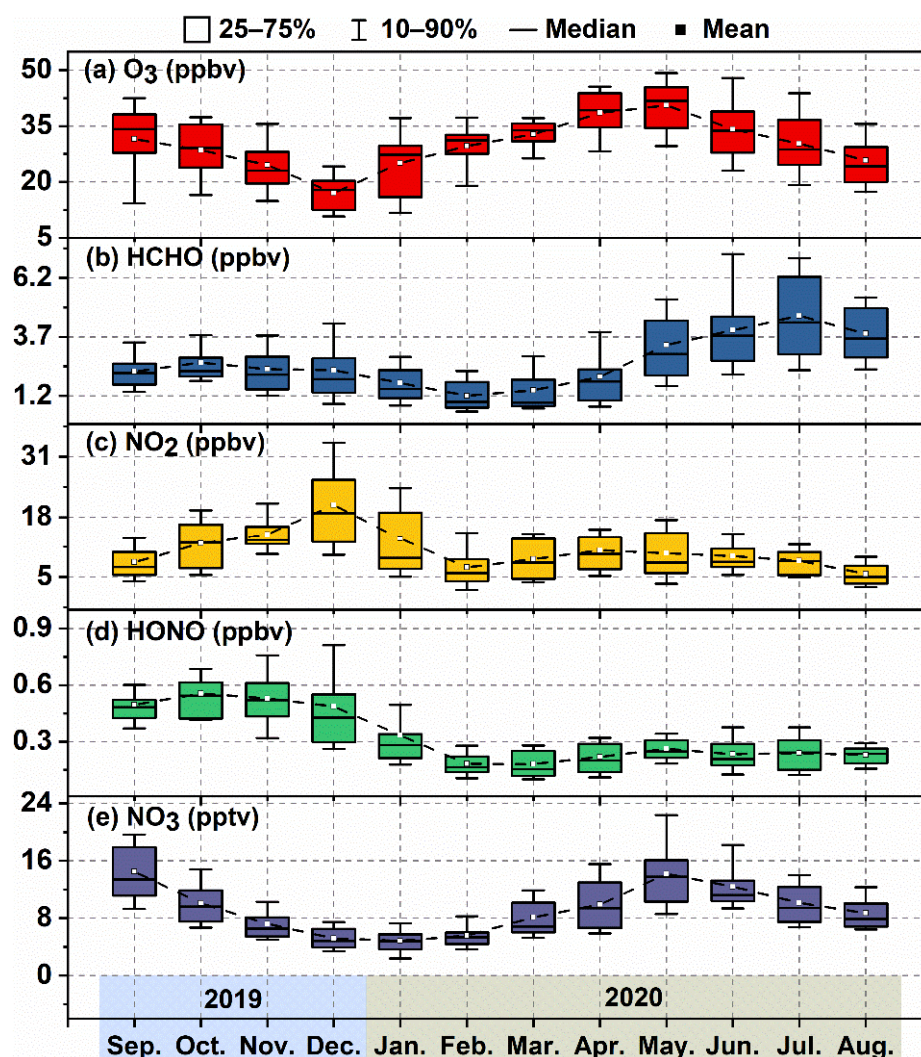

Figure 3. The monthly box charts of O_3 (**a**), HCHO (**b**), NO_2 (**c**), HONO (**d**), and NO_3 (**e**) from September 2019 to August 2020 in Nanhui, Shanghai. The monthly means are connected by black dotted lines.

During the one-year observation period, there was a high concentration of NO_3 radicals in the atmosphere in spring 2020, but a low concentration in winter 2019, depicting a trend similar to that of O_3. Given that O_3 and NO_2 are the precursors of NO_3 in the atmosphere and that the monthly variation in NO_3 synchronized with O_3, this indicated that the production of NO_3 was regulated more by O_3 than by NO_2 at the observation site.

The diurnal variations in hourly O_3, HCHO, NO_2, HONO, and NO_3 over the year were averaged as shown in Figure 4. O_3 and HCHO manifested coincident diurnal single-peak trends with maximums of 42.35 and 2.91 ppbv at 14:00 and 12:00, respectively. The marked generation during the daytime implied that these species maintained rich secondary sources. The stage during which O_3 levels declined before 06:00 was due to the titration effect caused by the increasing NO during rush hour when the generation of O_3 was comparatively weak [33]. On average, O_3 varied by 23.95 ppbv over a day, i.e., more than 100% of the daily minimum, while the variation in HCHO concentrations was 0.99 ppbv, i.e., approximately 50% of the daily minimum.
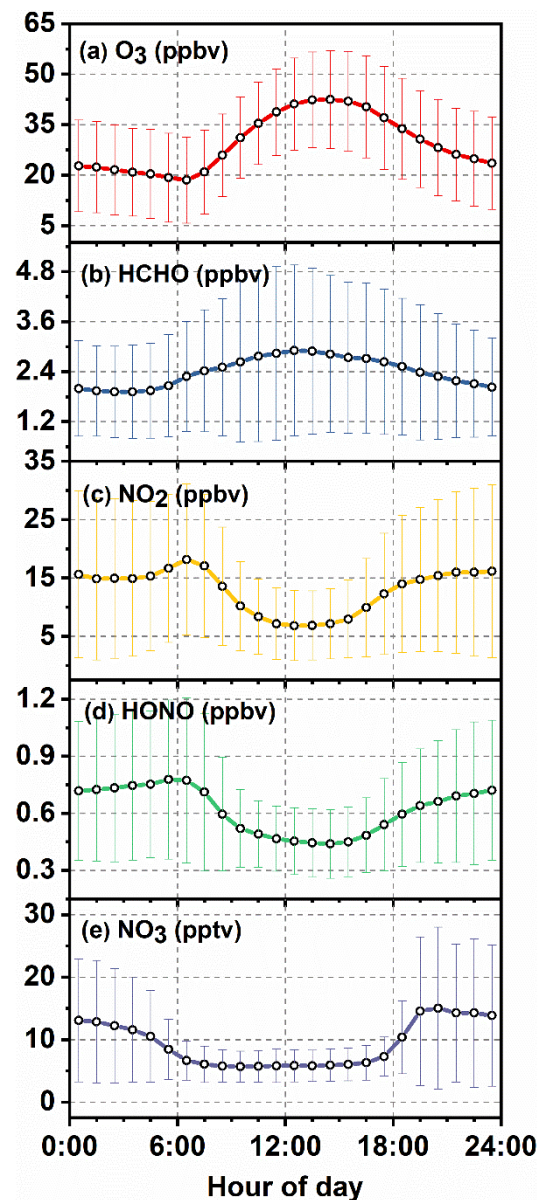
Figure 4. The mean diurnal variations in O_3 (**a**), HCHO (**b**), NO_2 (**c**), HONO (**d**), and NO_3 (**e**) from September 2019 to August 2020 in Nanhui, Shanghai. (The error bars indicate the standard deviations).

In contrast, the diurnal variations in NO_2 and HONO exhibited single-valley trends with minimums of 6.84 and 0.44 ppbv at 12:00 and 14:00, respectively. Vehicle emissions contributed to the anthropogenic primary sources during the morning rush hour, which led to a slight increase in the concentrations of these species. With respect to NO_3, the extreme photolysis during the daytime brought about a sustained minimal atmospheric concentration. After sunset, the NO_3 concentration increased rapidly to its maximum level at 20:00. The average nighttime NO_3 concentration reached 15 pptv, which was slightly lower than that observed in Shanghai in 2011 [34]. This phenomenon may be attributed to the current decrease in the precursors NO_2 and O_3.

3.2. Clustering of O_3 Diurnal Patterns

Admittedly, averaging over a time scale is a vital and traditional means to assess the temporal characteristics of pollutants. However, as discussed above, higher O_3 levels at this observation site were found not only in summer, but also in spring and autumn. Seasonal categories could not integrally reflect the features of higher O_3 conditions. In

response, we aimed to discard the time limit and classify the O_3 pollution based only on the characteristics of the daily O_3 variation. Accordingly, K-means clustering methodology was used to identify groups of O_3 pollution according to diurnal patterns, which enabled data objects to be assigned to the same cluster in accordance with common features [35]. Simultaneously, each cluster maintained distinct characteristics. Clustering analysis has been applied in atmospheric pollution for many years, especially using backward trajectory clustering [36].

    Here, we defined the number of clustering units as four. Detailed information including determination of the optimal cluster number, the process of clustering, and evaluation of the clustering result, can be found in the Supplementary Materials. Visualization of the clustering results is displayed in Figure 5a. The monthly distribution of all the clusters were shown in Figure S6. Clusters 1 and 4 appeared more in autumn, spring and summer, i.e., the O_3 pollution season in Shanghai. Additionally, cluster 3 appeared more in autumn and winter, whereas the distribution of cluster 2 was dispersed. The final four clustering centers shown in Figure 5b were used for the subsequent discussion. Additionally, the nighttime was divided into two parts, i.e., before (18:00–24:00) and after (00:00–06:00) midnight.
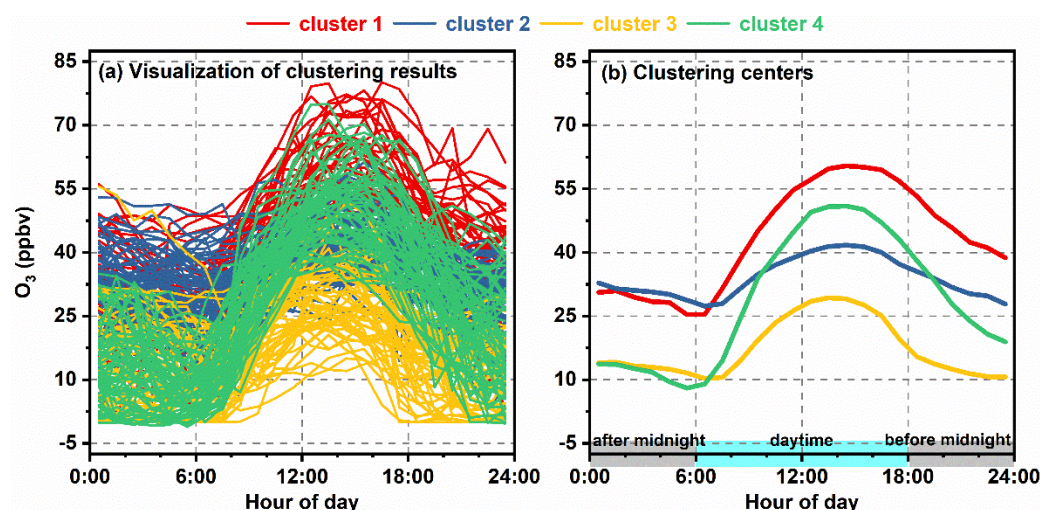

Figure 5. Visualization of the clustering results (**a**) and the final four clustering centers of the O_3 diurnal pattern (**b**).

    The O_3 for cluster 1 retained a higher level after midnight and a higher production during the daytime. At the end of the daily cycle, daily accumulation was observed instead of backtracking to the original level. Similarly, cluster 2 was characterized by a higher nighttime background; however, its daytime generation was weak. In addition, the O_3 concentration returned to the original level over a one-day period. Regarding cluster 3, the period after midnight revealed a relatively lower O_3 concentration compared to clusters 1 and 2. After sunrise, the daytime increase was small, and the concentration just before midnight was equal to the daily minimum, which paralleled cluster 2. Cluster 4 reflected a lower level after midnight, but a considerable increase during the daytime, whereas before midnight, it dropped rapidly and eventually presented an increase of about 10 ppbv over a one-day period.

    After identification of the four O_3 diurnal pattern clusters, in order to explore the drivers of the O_3 variations for the three different periods, relevant atmospheric components and meteorological factors for each cluster were averaged accordingly as illustrated in Figure 6. Furthermore, Table 1 briefly summarizes the information from Figure 6 for the four clusters in the different periods.

    As shown in Figure 6a, the period after midnight produced an O_3 gap of about 20 ppbv between clusters 1 and 2 and clusters 3 and 4. There was almost no O_3 generation chemically at night, during which the response of the meteorological factors to the O_3

concentration between clusters 1 and 2 and clusters 3 and 4 was indistinct, as shown in Figure 6. Therefore, the gap was considered to be the outcome of a depletion effect on the process of nocturnal atmospheric chemistry. Clusters 3 and 4 retained higher NO levels compared to clusters 1 and 2, as denoted in Figure 6e. Ambient NO reacted violently with O_3 and was capable of accelerating the O_3 consumption [37]. Therefore, NO was regarded as the driver of the O_3 gap in this period.
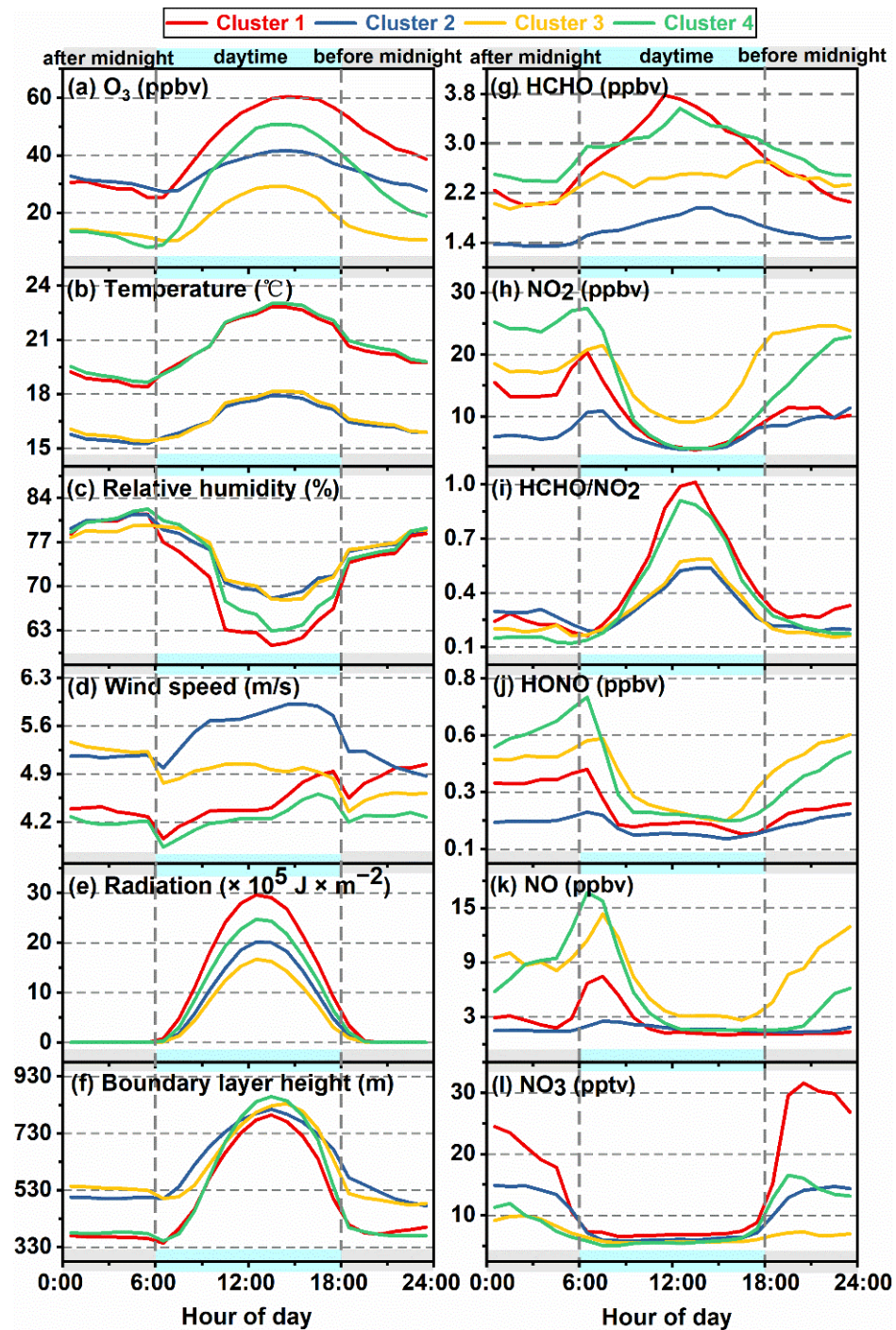

Figure 6. Diurnal variations in O_3 (**a**) and the meteorological factors (temperature (**b**), relative humidity (**c**), wind speed (**d**), radiation (**e**), and boundary layer height (**f**)) as well as the relevant atmospheric components (HCHO (**g**), NO_2 (**h**), HCHO/NO_2 (**i**), HONO (**j**), NO (**k**), and NO_3 (**l**)).

Table 1. A summary of the information visualized in Figure 6 for the four clusters in different periods.

Period	Species	Cluster 1	Cluster 2	Cluster 3	Cluster 4
After midnight	O_3 level	higher	higher	lower	lower
	NO titration	weak	weak	intense	intense
	HONO level	lower	//	//	higher
Daytime	O_3 increase	lower	//	//	higher
	Photochemical level	intense	weak	weak	intense
	Meteorological factors for photochemical reaction (T, RH, WS, R)	favorable	adverse	adverse	favorable
Before midnight	O_3-18:00	higher	//	//	lower
	max-NO_3	higher	//	//	lower
	BLH	lower	higher	higher	lower
	O_3 accumulation	yes	/	/	yes

T, RH, WS, R, and BLH represent temperature, relative humidity, wind speed, radiation, and boundary layer height, respectively. "/" represents a null value, while "//" in clusters 2 and 3 indicates that it is not discussed in this study.

During the daytime, the photochemical generation of O_3 suggested a prominent difference between clusters 1 and 4 and clusters 2 and 3. Intense photochemical reactions (clusters 1 and 4) were detected accompanied by higher temperature, lower relative humidity, lower wind speed, and higher radiation, which accorded with the basic understanding of the photochemical reactions and has also been verified in previous studies [38,39]. With respect to precursors of photochemistry, the dominant roles of HCHO and NO_2 in the generation of O_3 cannot be neglected since it was confirmed that HCHO and NO_2 are able to characterize the respective levels of VOCs and NO_x in the atmosphere [40]. However, they displayed completely different behavior toward O_3 variation (Figure 6g,h): HCHO was apparently higher for clusters 1 and 4 associated with evident O_3 production, while NO_2 was difficult to distinguish among them. This implied that the photochemical generation of O_3 was basically dominated by VOCs rather than NO_x in Shanghai, which has also been reported in previous studies [41,42].

The dependences of O_3 on HCHO, HCHO/NO_2, and NO_x were surveyed as depicted in Figure 7. O_3 concentration was found to correlate with HCHO for all clusters except for the low O_3 cluster 3. Moreover, O_3 correlated with HCHO/NO_2, but negatively correlated with NO_x for all clusters. For cluster 3, a strong negative correlation with NO_x resulted in the good correlation with HCHO/NO_2 in the case that the correlation with HCHO was poor. This provided important information for O_3 control strategies.

Compared to the time after midnight, a more significant decline in surface O_3 was revealed before midnight. This period indicated the diverse terminuses of the four clusters over the daily cycle. The O_3 concentration for clusters 1 and 4 exhibited a certain accumulation, while clusters 2 and 3 regressed to the level of the daily minimum. Lower boundary layer heights were discovered for clusters 1 and 4 (Figure 6f), which directly hindered O_3 diffusion and further led to the slow decline in ambient O_3. Therefore, the boundary layer height seemed to be the driver of the O_3 decline before midnight.

3.3. Interactions of Day- and Nighttime Atmospheric Components

In this section, we discuss the interactions among the three periods by taking the daytime period as the object. We investigated the impact of the period after midnight on the daytime as well as how it affected the period before midnight. Since the daytime was characterized by intense photochemical generation of O_3, clusters 1 and 4 were suitably selected for the subsequent discussion.

The HONO levels of clusters 1 and 4 showed disparity after midnight (Figure 6j). After sunrise, the atmospheric HONO decreased rapidly because of the escalation of photolysis. The higher HONO level for cluster 4 resulted in a more prominent photochemistry as denoted by the more elevated O_3 during the daytime in Figure 6a. The photolysis of

HONO is an important source of OH radicals in the atmosphere [43,44]. HONO is able to significantly enhance the oxidation capacity of the atmosphere and further promote the photochemical generation of O_3 [45,46].
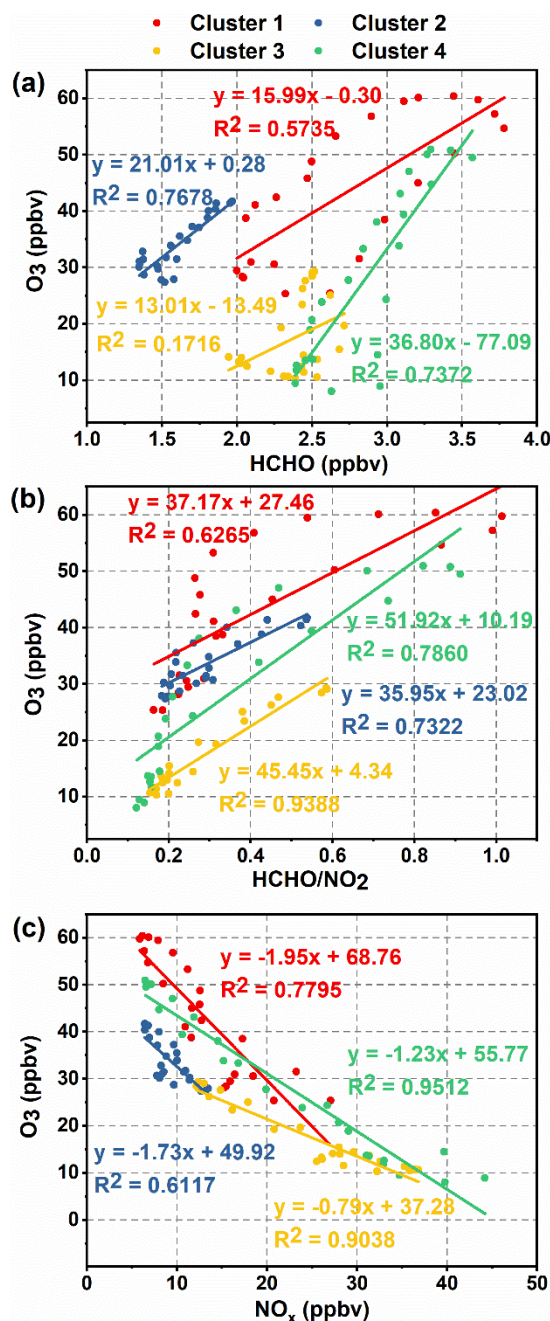

Figure 7. The O_3 concentrations and corresponding HCHO concentrations (**a**), HCHO/NO_2 ratios (**b**), and NO_x concentrations (**c**) for the four clusters. Colored lines represent the linear fit for each cluster.

The radiation for cluster 4 was found to be lower than that for cluster 1 during the daytime (Figure 6e); meanwhile, the O_3 increase in cluster 4 was larger than that in cluster 1. We accordingly explored the influence of the radiation on HONO-O_3 levels, as illustrated in Figure 8. When the radiation was higher, the daytime O_3 increment showed the most sensitive reaction to the variation in averaged HONO after midnight, with a slope of 47.16. As radiation dropped to the middle level, the sensitivity was hence reduced, whereas the response between the O_3 increment and the averaged HONO was unclear when radiation was lower than 2.6×10^6 J·m^{-2}. Figure 8b shows the proportions of radiation levels in

clusters 1 and 4. It is obvious that cluster 1 was more occupied by higher radiation while lower radiation mainly covered cluster 4. Consequently, for cluster 4, it was not surprising to find the larger O_3 increment even though the radiation was relatively low.
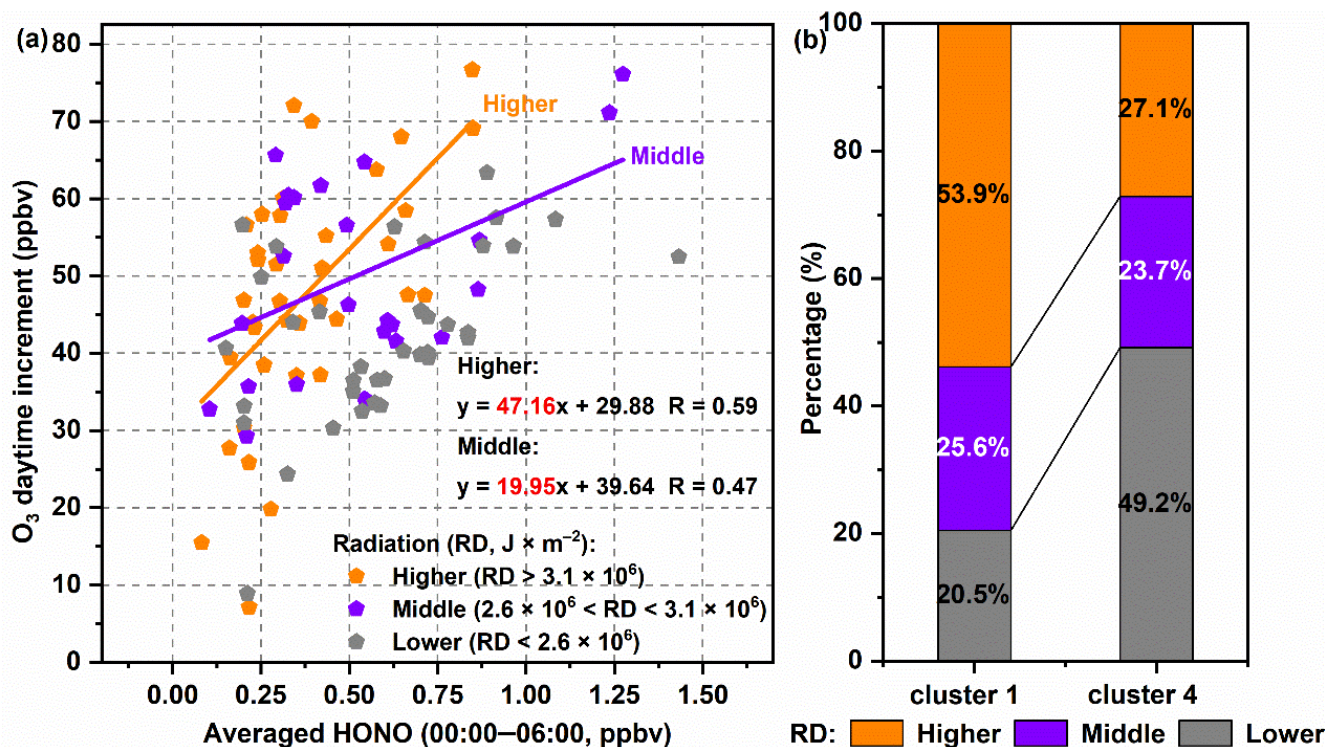

Figure 8. The dependence of the O_3 increment in clusters 1 and 4 on the HONO concentration under different radiation conditions (**a**) and the radiation distributions of clusters 1 and cluster 4 (**b**).

In terms of daytime O_3 acting in the nighttime atmosphere, the NO_3 level for clusters 1 and 4 was found to reflect a final gap of 16 pptv before midnight (Figure 6l), which could be attributed to the O_3 difference after sunset. The larger remnant of O_3 for cluster 1 in the daytime facilitated the generation of NO_3 before midnight. NO_3 is a crucial oxidant in the nocturnal atmosphere [19], which can trigger the conversion of a variety of VOCs, and NO_x can also be removed from the atmosphere by further forming soluble nitrates after conversion into NO_3 [47,48]. Therefore, the higher daytime O_3 seemed to play a critical role in various nocturnal atmospheric chemical processes by generating more NO_3.

Moreover, the relationship between the daily O_3 concentration at 18:00 and the maximum NO_3 before midnight was investigated (Figure 9). The O_3 level at 18:00 was considered the endpoint of generation and loss during the daytime. Overall, max-NO_3 exhibited an exponential growth with O_3-18:00, suggesting that the increase tended to be faster gradually. Cluster 1 evidently experienced a steeper rise than cluster 4 owing to the larger persistent level of O_3 in the daytime.

Furthermore, in order to explore O_3 pollution associated with the meteorological conditions and the corresponding variability of the relative atmospheric components at a more detailed level, a case study of a high O_3 pollution episode was carried out as shown in Supplementary Materials (Figure S7, Table S2). The in-depth analysis of the case study is also found to be consistent with the clustering characteristics.
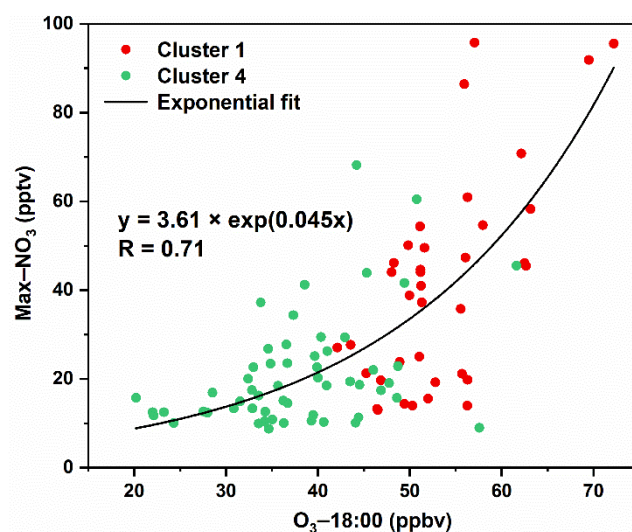
Figure 9. The daily O_3 concentration at 18:00 and the maximum concentration of NO_3 between 18:00 and 23:00 in clusters 1 and 4.

4. Conclusions

The current study surveyed O_3, HCHO, NO_2, HONO and NO_3 concentrations from September 2019 to August 2020 based on LP-DOAS measurements in Nanhui, Shanghai. Here, we classified O_3 diurnal patterns into four clusters using the K-means clustering methodology, the differences among which were manifested in three periods: daytime and before and after midnight. The relevant atmospheric components and meteorological factors were examined purposefully.

The period after midnight showed an evident O_3 gap between clusters 1 and 2 and clusters 3 and 4, which was driven by different ambient NO. During the daytime, the intense photochemistry was found to strongly depend on the meteorological conditions of higher temperature, lower humidity, lower wind speed and higher radiation. O_3 correlated with HCHO/NO_2, but negatively correlated with NO_x for all clusters. The HCHO/NO_2 ratio was an excellent indicator of the O_3 levels rather than HCHO itself. Moreover, the lower boundary layer height before midnight seemed to hinder the diffusion of O_3, which resulted in an accumulation at the end of the daily cycle. The interactions among the three periods of the diurnal pattern were analyzed for clusters 1 and 4. The daytime O_3 levels showed a consensus with the HONO levels after midnight, during which time radiation conditionally played a role. In addition, the cumulative O_3 in the daytime determined the level of NO_3 production before midnight.

As the DOAS method can simultaneously detect multiple trace gases in the atmosphere, we determined that the relationship between active atmospheric components and O_3 pollution can be reviewed from the perspective of diurnal interaction. Therefore, this paper provides novel inspiration for the future study and management of regional O_3 pollution.

Supplementary Materials: The following supporting information can be downloaded at: https://www.mdpi.com/article/10.3390/atmos13020351/s1. Table S1. DOAS fit settings and detection limits for O_3, NO_2, HCHO, HONO and NO_3; Table S2. A summary of the relevant atmospheric components for each day; Figure S1. Time series of the O_3 and NO_2 mixing ratios of the DOAS retrieval, and the linear fitting, mean bias and the standard deviation for the two observation methods; Figure S2. DBI values for the number of clusters from 1 to 10. Figure S3. The process of clustering in this study; Figure S4. Bar plots of the silhouette coefficient values for all the diurnal patterns; Figure S5. The SC values when the cluster number is defined range from 2 to 10; Figure S6. The monthly distribution of clustering result; Figure S7. Time series of O_3, HCHO and NO_2, HCHO/NO_2 and NO, NO_3 and HONO, temperature (T) and relative humidity (RH), wind speed (WS), boundary layer height (BLH) and radiation (R).

References

1. Qiu, W.Y.; Li, S.L.; Liu, Y.H.; Lu, K.D. Petrochemical and industrial sources of volatile organic compounds analyzed via regional wind-driven network in Shanghai. *Atmosphere* **2019**, *10*, 760. [CrossRef]
2. Zhang, J.; Li, D.; Bian, J.; Bai, Z. Deep stratospheric intrusion and Russian wildfire induce enhanced tropospheric ozone pollution over the northern Tibetan Plateau. *Atmos. Res.* **2021**, *259*, 105662. [CrossRef]
3. Alejandro, S.; Valdes, H.; Zaror, C.A. Natural zeolite reactivity towards ozone: The role of acid surface sites. *Adv. Oxid. Technol. J.* **2011**, *14*, 182–189. [CrossRef]
4. Schnell, J.L.; Prather, M.J.; Josse, B.; Naik, V.; Horowitz, L.W.; Zeng, G.; Shindell, D.T.; Faluvegi, G. Effect of climate change on surface ozone over North America, Europe, and East Asia. *Geophys. Res. Lett.* **2016**, *43*, 3509–3518. [CrossRef] [PubMed]
5. Unger, N.; Zheng, Y.Q.; Yue, X.; Harper, K.L. Mitigation of ozone damage to the world's land ecosystems by source sector. *Nat. Clim. Chang.* **2020**, *10*, 134–137. [CrossRef]
6. Li, K.; Jacob, D.J.; Liao, H.; Shen, L.; Zhang, Q.; Bates, K.H. Anthropogenic drivers of 2013–2017 trends in summer surface ozone in China. *Proc. Natl. Acad. Sci. USA* **2019**, *116*, 422–427. [CrossRef]
7. Wang, T.; Xue, L.; Brimblecombe, P.; Lam, Y.F.; Li, L.; Zhang, L. Ozone pollution in China: A review of concentrations, meteorological influences, chemical precursors, and effects. *Sci. Total Environ.* **2017**, *575*, 1582–1596. [CrossRef]
8. Liu, P.F.; Song, H.Q.; Wang, T.H.; Wang, F.; Li, X.Y.; Miao, C.H.; Zhao, H.P. Effects of meteorological conditions and anthropogenic precursors on ground-level ozone concentrations in Chinese cities. *Environ. Pollut.* **2020**, *262*, 8. [CrossRef]
9. Wang, N.; Lyu, X.P.; Deng, X.J.; Huang, X.; Jiang, F.; Ding, A.J. Aggravating O_3 pollution due to NO_x emission control in eastern China. *Sci. Total Environ.* **2019**, *677*, 732–744. [CrossRef] [PubMed]
10. Chen, Z.Y.; Li, R.Y.; Chen, D.L.; Zhuang, Y.; Gao, B.B.; Yang, L.; Li, M.C. Understanding the causal influence of major meteorological factors on ground ozone concentrations across China. *J. Clean. Prod.* **2020**, *242*, 13. [CrossRef]
11. Chen, Z.Y.; Zhuang, Y.; Xie, X.M.; Chen, D.L.; Cheng, N.L.; Yang, L.; Li, R.Y. Understanding long-term variations of meteorological influences on ground ozone concentrations in Beijing During 2006–2016. *Environ. Pollut.* **2019**, *245*, 29–37. [CrossRef] [PubMed]
12. Shan, W.P.; Yin, Y.Q.; Zhang, J.D.; Ji, X.; Deng, X.Y. Surface ozone and meteorological condition in a single year at an urban site in central-eastern China. *Environ. Monit. Assess.* **2009**, *151*, 127–141. [CrossRef] [PubMed]
13. Yan, J.J.; Wang, G.L.; Yang, P.C. Study on the Sensitivity of Summer Ozone Density to the Enhanced Aerosol Loading over the Tibetan Plateau. *Atmosphere* **2020**, *11*, 138. [CrossRef]
14. Yu, D.; Tan, Z.; Lu, K.; Ma, X.; Li, X.; Chen, S.; Zhu, B.; Lin, L.; Li, Y.; Qiu, P.; et al. An explicit study of local ozone budget and NOx-VOCs sensitivity in Shenzhen China. *Atmos. Environ.* **2020**, *224*, 13. [CrossRef]
15. Sun, L.Q.; Cheng, K.X.; Yang, H.D.; He, Q.S. An on-line monitoring technique for Trace Gases in Atmosphere Based on Differential optical absorption spectroscopy. In Proceedings of the 2nd Conference of the Optics-and-Photonics-Society-of-Singapore/International Conference on Optics in Precision Engineering and Nanotechnology (icOPEN), Singapore, 9–11 April 2013; Volume 8769.
16. Allegrini, I.; Febo, A.; Giliberti, C.; Perrino, C. Intercomparison of DOAS and conventional analysers in the measurement of atmospheric pollutants in an urban background monitoring site of Rome. In Proceedings of the Conference on Remote Sensing of Vegetation and Water, and Standardization of Remote Sensing Methods, Munich, Germany, 18–19 June 1997; Volume 3107, pp. 64–73.
17. Hoffman, S.; Sulkowski, W.; Krzyzanowski, K. The urban ozone monitoring by the DOAS technique application. *J. Mol. Struct.* **1995**, *348*, 187–189. [CrossRef]
18. Zhu, J.; Wang, S.S.; Wang, H.L.; Jing, S.G.; Lou, S.R.; Saiz-Lopez, A.; Zhou, B. Observationally constrained modeling of atmospheric oxidation capacity and photochemical reactivity in Shanghai, China. *Atmos. Chem. Phys.* **2020**, *20*, 1217–1232. [CrossRef]
19. Yan, Y.H.; Wang, S.S.; Zhu, J.; Guo, Y.L.; Tang, G.Q.; Liu, B.X.; An, X.X.; Wang, Y.S.; Zhou, B. Vertically increased NO_3 radical in the nocturnal boundary layer. *Sci. Total Environ.* **2021**, *763*, 12. [CrossRef]

20. Voigt, S.; Orphal, J.; Burrows, J.P. The temperature and pressure dependence of the absorption cross-sections of NO$_2$ in the 250–800 nm region measured by Fourier-transform spectroscopy. *J. Photochem. Photobiol. A-Chem.* **2002**, *149*, 1–7. [CrossRef]

21. Meller, R.; Moortgat, G.K. Temperature dependence of the absorption cross sections of formaldehyde between 223 and 323 K in the wavelength range 225–375 nm. *J. Geophys. Res.-Atmos.* **2000**, *105*, 7089–7101. [CrossRef]

22. Hermans, C.; Vandaele, A.C.; Fally, S. Fourier transform measurements of SO2 absorption cross sections: I. Temperature dependence in the 24,000–29,000 cm^{-1} (345–420 nm) region. *J. Quant. Spectrosc. Radiat. Transf.* **2009**, *110*, 756–765. [CrossRef]

23. Stutz, J.; Kim, E.S.; Platt, U.; Bruno, P.; Perrino, C.; Febo, A. UV-visible absorption cross sections of nitrous acid. *J. Geophys. Res.-Atmos.* **2000**, *105*, 14585–14592. [CrossRef]

24. Voigt, S.; Orphal, J.; Bogumil, K.; Burrows, J.P. The temperature dependence (203–293 K) of the absorption cross sections of O$_3$ in the 230–850 nm region measured by Fourier-transform spectroscopy. *J. Photochem. Photobiol. A-Chem.* **2001**, *143*, 1–9. [CrossRef]

25. Wu, J.; Xiao, B. Study on near-surface ozone pollution in Shanghai urban area. *Guangzhou Chem. Ind.* **2020**, *48*, 112–116, 156.

26. Xu, J.M.; Tie, X.X.; Gao, W.; Lin, Y.F.; Fu, Q.Y. Measurement and model analyses of the ozone variation during 2006 to 2015 and its response to emission change in megacity Shanghai, China. *Atmos. Chem. Phys.* **2019**, *19*, 9017–9035. [CrossRef]

27. Tang, G.; Liu, Y.; Zhang, J.; Liu, B.; Li, Q.; Sun, J.; Wang, Y.; Xuan, Y.; Li, Y.; Pan, J.; et al. Bypassing the NOx titration trap in ozone pollution control in Beijing. *Atmos. Res.* **2021**, *249*, 105333. [CrossRef]

28. Zhang, J.; Li, D.; Bian, J.; Xuan, Y.; Chen, H.; Bai, Z.; Wan, X.; Zheng, X.; Xia, X.; Lu, D. Long-term ozone variability in the vertical structure and integrated column over the North China Plain: Results based on ozonesonde and Dobson measurements during 2001–2019. *Environ. Res. Lett.* **2021**, *16*, 074053. [CrossRef]

29. Guo, Y.L.; Wang, S.S.; Zhu, J.; Zhang, R.F.; Gao, S.; Saiz-Lopez, A.; Zhou, B. Atmospheric formaldehyde, glyoxal and their relations to ozone pollution under low- and high-NOx regimes in summertime Shanghai, China. *Atmos. Res.* **2021**, *258*, 10. [CrossRef]

30. Chen, Y.Y.; Bai, Y.; Liu, H.T.; Alatalo, J.M.; Jiang, B. Temporal variations in ambient air quality indicators in Shanghai municipality, China. *Sci. Rep.* **2020**, *10*, 11. [CrossRef]

31. Li, D.D.; Xue, L.K.; Wen, L.; Wang, X.F.; Chen, T.S.; Mellouki, A.; Chen, J.M.; Wang, W.X. Characteristics and sources of nitrous acid in an urban atmosphere of northern China: Results from 1-yr continuous observations. *Atmos. Environ.* **2018**, *182*, 296–306. [CrossRef]

32. Tanvir, A.; Javed, Z.; Jian, Z.; Zhang, S.B.; Bilal, M.; Xue, R.B.; Wang, S.S.; Bin, Z. Ground-Based MAX-DOAS Observations of Tropospheric NO$_2$ and HCHO During COVID-19 Lockdown and Spring Festival Over Shanghai, China. *Remote Sens.* **2021**, *13*, 488. [CrossRef]

33. Fu, Z.Q.; Dai, C.H.; Wang, Z.W.; Guo, J.; Qin, P.F.; Zhang, X.S. Sensitivity analysis of atmospheric ozone formation to its precursors in summer of Changsha. *Environ. Chem.* **2019**, *38*, 531–538.

34. Wang, S.S.; Shi, C.Z.; Zhou, B.; Zhao, H.; Wang, Z.R.; Yang, S.N.; Chen, L.M. Observation of NO$_3$ radicals over Shanghai, China. *Atmos. Environ.* **2013**, *70*, 401–409. [CrossRef]

35. Govender, P.; Sivakumar, V. Application of k-means and hierarchical clustering techniques for analysis of air pollution: A review (1980–2019). *Atmos. Pollut. Res.* **2020**, *11*, 40–56. [CrossRef]

36. Darby, L.S. Cluster analysis of surface winds in Houston, Texas, and the impact of wind patterns on ozone. *J. Appl. Meteorol.* **2005**, *44*, 1788–1806. [CrossRef]

37. Awang, N.R.; Ramli, N.A.; Yahaya, A.S.; Elbayoumi, M. High Nighttime Ground-Level Ozone Concentrations in Kemaman: NO and NO2 Concentrations Attributions. *Aerosol Air Qual. Res.* **2015**, *15*, 1357–1366. [CrossRef]

38. An, J.L.; Hang, Y.X.; Zhu, B.; Wang, D.D. Observational study of ozone concentrations in northern suburb of Nanjing. *Ecol. Environ. Sci.* **2010**, *19*, 1383–1386.

39. Li, M.Y.; Yu, S.C.; Chen, X.; Li, Z.; Zhang, Y.B.; Wang, L.Q.; Liu, W.P.; Li, P.F.; Lichtfouse, E.; Rosenfeld, D.; et al. Large scale control of surface ozone by relative humidity observed during warm seasons in China. *Environ. Chem. Lett.* **2021**, *19*, 3981–3989. [CrossRef]

40. Hong, Q.Q.; Liu, C.; Hu, Q.H.; Zhang, Y.L.; Xing, C.Z.; Su, W.J.; Ji, X.G.; Xiao, S.X. Evaluating the feasibility of formaldehyde derived from hyperspectral remote sensing as a proxy for volatile organic compounds. *Atmos. Res.* **2021**, *264*, 12. [CrossRef]

41. Lin, H.T.; Wang, M.; Duan, Y.S.; Fu, Q.Y.; Ji, W.H.; Cui, H.X.; Jin, D.; Lin, Y.F.; Hu, K. O$_3$ sensitivity and contributions of different NMHC sources in O$_3$ formation at urban and suburban sites in Shanghai. *Atmosphere* **2020**, *11*, 295. [CrossRef]

42. Yang, L.F.; Yuan, Z.B.; Luo, H.H.; Wang, Y.R.; Xu, Y.Q.; Duan, Y.S.; Fu, Q.Y. Identification of long-term evolution of ozone sensitivity to precursors based on two-dimensional mutual verification. *Sci. Total Environ.* **2021**, *760*, 9. [CrossRef]

43. Alicke, B.; Geyer, A.; Hofzumahaus, A.; Holland, F.; Konrad, S.; Patz, H.W.; Schafer, J.; Stutz, J.; Volz-Thomas, A.; Platt, U. OH formation by HONO photolysis during the BERLIOZ experiment. *J. Geophys. Res.-Atmos.* **2003**, *108*, 17. [CrossRef]

44. Harris, G.W.; Carter, W.P.L.; Winer, A.M.; Pitts, J.N.; Platt, U.; Perner, D. Observations of nitrous-acid in the Los-Angeles atmosphere and implications for predictions of ozone precursor relationships. *Environ. Sci. Technol.* **1982**, *16*, 414–419. [CrossRef] [PubMed]

45. Fu, X.; Wang, T.; Zhang, L.; Li, Q.Y.; Wang, Z.; Xia, M.; Yun, H.; Wang, W.H.; Yu, C.; Yue, D.L.; et al. The significant contribution of HONO to secondary pollutants during a severe winter pollution event in southern China. *Atmos. Chem. Phys.* **2019**, *19*, 1–14. [CrossRef]

46. Jia, C.H.; Tong, S.R.; Zhang, W.Q.; Zhang, X.R.; Li, W.R.; Wang, Z.; Wang, L.L.; Liu, Z.R.; Hu, B.; Zhao, P.S.; et al. Pollution characteristics and potential sources of nitrous acid (HONO) in early autumn 2018 of Beijing. *Sci. Total Environ.* **2020**, *735*, 11. [CrossRef] [PubMed]
47. Brown, S.S.; Stutz, J. Nighttime radical observations and chemistry. *Chem. Soc. Rev.* **2012**, *41*, 6405–6447. [CrossRef]
48. Pye, H.O.T.; Chan, A.W.H.; Barkley, M.P.; Seinfeld, J.H. Global modeling of organic aerosol: The importance of reactive nitrogen (NO$_x$ and NO$_3$). *Atmos. Chem. Phys.* **2010**, *10*, 11261–11276. [CrossRef]